Research Square

Preprints are preliminary reports that have not undergone peer review.
They should not be considered conclusive, used to inform clinical practice,
or referenced by the media as validated information.

# Microstructure Organization and Composition of Argopecten purpuratus Scallop Shell

**Adrian Barry-Sosa**
Universidad de Granada - Campus Fuentenueva: Universidad de Granada
**Katarzyna Berent**
AGH University of Krakow: Akademia Gorniczo-Hutnicza im Stanislawa Staszica w Krakowie
**Laura Ramajo**
CEAZA: Centro de Estudios Avanzados en Zonas Aridas
**Nelson A. Lagos**
Universidad Santo Tomas
**Antonio G. Checa**
Universidad de Granada - Campus Fuentenueva: Universidad de Granada
**Alejandro B Rodriguez Navarro**
anava@ugr.es

Universidad de Granada - Campus Fuentenueva: Universidad de Granada

**Research Article**

**Keywords:**

**Posted Date:** March 12th, 2026

**DOI:** https://doi.org/10.21203/rs.3.rs-9010744/v1

**License:** This work is licensed under a Creative Commons Attribution 4.0 International License.
Read Full License

# Abstract

The scallop *Argopecten purpuratus* is distributed alongside the coast of Peru and Chile, representing a key species in the aquaculture industry, with significant socioeconomic importance due to its high level of worldwide exports. While several studies have addressed how this species responds to environmental changes aiming to increase industry relevant traits like growth, its shell microstructure has not yet been well described. This aspect is key for understanding how potential environmental changes, such as ocean acidification, may affect the species. In this study, we show that *A. purpuratus* shell has a three-layered structure. The outer layer is made of granular calcite crystals, followed by a second layer underneath composed of small platy crystals arranged in packs with coherent crystallographic orientation, which gives the impression of large grains under EBSD. The third and thickest layer consists of foliated calcite arranged in sheets with alternating directions. This general scheme is altered towards the dorsal shell side, with the presence of the prismatic aragonitic myostracum intersecting those layers, and the addition of a complex cross-foliated layer underneath. Overall, this study provides key data on the shell microstructure of *A. purpuratus*, forming a foundation for future studies focused on this vital structure for the organism´s survival, particularly in the context of ongoing current climate change.


# Introduction

*Argopecten purpuratus* (Lamarck 1819) is a bivalve that belongs to the family Pectinidae, distributed alongside the Pacific coast of Peru and Chile from 5º S to 30º S (Wolff and Mendo, 2000). It is an epibenthic bivalve that inhabits a variety of substrates, including stone, sand and mud at depths ranging from 5 to 40 m (Acosta-Jofré et al. 2020). This species is exclusively marine and does not tolerate low salinity environments, where its survival gets compromised (Fernández-Reiriz et al. 2005; Soria et al. 2007; Brand 2016). However, it is well-adapted to environmental fluctuations in temperature, pH and oxygen concentrations, such as those driven by upwelling (Ramajo et al. 2016, 2020, 2022). In addition, recent studies state that under current conditions, *A. purpuratus* populations are strong, as evidenced by their high genetic diversity (Acosta-Jofré et al. 2020; Marín et al. 2013).

*A. purpuratus* is a species of key economic importance, representing a significant portion of fishery and aquaculture industries in both Chile and Peru. Recent data show that this species has supported annual productions reaching 4,171 tons in Chile (Sernapesca 2024), and 43,006 tons in Peru (Mendo et al. 2016; Bakit et al. 2024; Produce 2025). To date, due to its socioeconomic relevance, a wealth of studies exists on this species, even being one of the few bivalves that has its genome sequenced (Li et al. 2018). Additionally, numerous studies over recent decades have aimed to understand the physiological limits of this species in order to explain fluctuations in landings associated with environmental changes driven by El Niño-La Niña oscillations (ENSO) and/ or upwelling events (Taylor et al. 2008; Yáñez et al. 2017). In Chile and Peru, *A. purpuratus* is subjected to regular environmental changes due to seasonal or permanent upwelling events which modulate temperature, pH, dissolved oxygen and primary productivity (Ramajo et al. 2020, 2022; Muñoz et al. 2023). Recent studies have observed that the magnitude of pH changes linked to upwelling conditions is comparable to pH values predicted globally under ocean

acidification or ocean deoxygenation scenarios (Ramajo et al. 2016; Lagos et al. 2021). Furthermore, many studies declare that living under fluctuating and often stressful environmental conditions has endowed *A. purpuratus* with a set of biological mechanisms, such as increased periostracum thickness to avoid shell dissolution (Ramajo et al. 2016, 2025). Studies have also determined that food availability promotes the expression of biological mechanisms and phenotypic plasticity in several traits, allowing this species not only to be highly adapted to current environmental conditions, but also to increase its resilience to changes induced by climate change (Ramajo et al. 2016, 2022, 2025).

Related to shell biomineralization impacts, it has been shown that the combined effect of low temperatures (around 14 ºC), and low pH, induces a decrease in shell growth rates and net shell dissolution (Lagos et al. 2016). The effect of decreased pH is partially mitigated by warmer (~ 18 ºC) temperatures (Lagos et al. 2016). At lower pH, *A. purpuratus* experiences changes in shell calcification rates, shell organic matrix and mineral organization but it can maintain its shell biomechanical properties (Lagos et al., 2021; Ramajo et al., 2020). Shell microhardness has also been observed to increase under low pH conditions (Córdova-Rodríguez et al. 2022). Additionally, the response of individuals to a changing environment is highly dependent on their life stage (larvae, juvenile or adult), with early stages generally being more susceptible (Ramajo et al. 2022).

However, despite all these studies, the *A. purpuratus* shell, a key element for the organism's survival, has not been characterized in sufficient detail. Thus, the main goal of this study is to provide the first detailed description of *A. purpuratus* shell chemical composition, mineralogy and microstructure, using complementary analytical techniques such as optical microscopy, scanning electron microscopy coupled with electron backscatter diffraction (SEM-EBSD), transmission electron microscopy (TEM), thermogravimetric analysis (TGA), Fourier transform infrared spectroscopy (FTIR), X-ray diffraction (XRD), and inductively coupled plasma optical emission spectroscopy **(**ICP-OES). Filling this fundamental knowledge gap is crucial for further studies on this relevant species and its responses to current and future environmental changes.

# Material and Methods

### Sample collection and preparation

Samples of *A. purpuratus* were collected on OSTIMAR S.A. culture line (30°16'49.4"S; 71°34'03.7"W; Chilean coast) at 9 m of depth. Individual dorsoventral diameters ranged from 40 to 90 mm in length (see Ramajo et al. 2022 for more information).

### Optical microscopy

Thin sections (< 30 µm) of shell samples were prepared for optical microscopy cut across the longitudinal (umbo to growth margin) and transversal (parallel to the growth margin) axes. Thin sections were observed using a Carl Zeiss Jenapol-U optical microscope equipped with a Nikon D7000 digital camara under transmitted and polarized light.

**X-Ray diffraction (DRX)**

Powdered shell samples from three individuals were analyzed in reflection mode with a PANanalytics Xpert Pro X-Ray diffractometer using Cu Ka radiation (λ = 1.5406 Å) before and after heating at 400 ºC. The theta-2Theta scans were measured from 5 to 80º with a step size of 0.017º and an integration time per step of 69.85 s. Rietveld refinement was performed on the resulting data using the TOPAS 5.0 software (Bruker, Germany). Additionally, for 8 samples, 1x1 cm shell pieces were cut and selected for pole figures analysis. Measurements were carried out using an X-ray single crystal diffractometer D8 Venture (Bruker, Germany) equipped with a Photon 100 detector, a Mo X-ray source (λ = 0.711 Å), and a 0.2 mm collimator.

**Electron microscopy**

Longitudinal and transversal cross-sections of shell samples were visualized using scanning electron microscopy (SEM). They were prepared by polishing the sample surface and then briefly etching with a solution of 0.05 M ethylenediaminetetraacetic acid (EDTA), and 0.25 M 4-(2-hydroxyethyl)-1-piperazineethanesulfonic acid (HEPES) buffer, to reveal the crystal outlines. Sections were then mounted on stubs and carbon coated. Secondary electron (SE) and backscattered electron (BSE) images were obtained using both a Phenom XL (Thermo Fisher) and a Quanta 400 ESEM (FEI). Energy dispersive X-ray (EDX) analyses were done using a detector (XFlash 6/30, Bruker Germany), mounted on the latter instrument, on the shell surface at locations with and without periostracum. Instruments are located at the Centro de Instrumentación Científica, Universidad de Granada (CIC, UGR).

To analyze the periostracum morphology by transmission electron microscope (TEM), small shell fragments (1x1 mm) close to the growth margin were cut and demineralized with 0.05M EDTA. The resulting film-like periostracum was included in resin, cut with an ultramicrotome (LEICA Ultracut R) and observed in a Zeiss Libra 120 Plus TEM (Carl Zeiss).

**Electron Backscatter Diffraction (EBSD)**

To analyze *A. purpuratus* shell microstructure, electron backscatter diffraction (EBSD) analysis was used to characterize crystal orientation in shells from two individuals. Shell fragments were embedded in epoxy resin and cut perpendicular to the shell surface, either along a direction starting from the umbo and ending at the shell margin (longitudinal cross-section) or parallel to the shell margin (transversal cross-section). The sections were ground using a series of silicon carbide papers of progressively finer grit sizes, followed by final polishing with colloidal silica to obtain a smooth surface. EBSD measurements were carried out using a Versa 3D FESEM (FEI), equipped with a Symmetry S2 camera (Oxford Instruments) and operated at an acceleration voltage of 12 kV. EBSD maps were collected at 1 µm step size. The data collected were analyzed using Aztec 6.0 software (Oxford Instruments). For each measurement, the region of interest (ROI) was divided into 6 areas of the same surface area to investigate microstructural/crystallographic texture changes.

### Fourier Transformed Infrared Spectroscopy (FTIR)

The chemical composition of the periostracum was determined by analyzing the outer shell surface by Attenuated Total Reflectance-Fourier Transformed Infrared Spectroscopy (ATR-FTIR) (Jasco Model 6600 FTIR spectrometer). A total of 32 scans with a resolution of 2 $cm^{-1}$ were collected.

### Thermogravimetric analysis (TGA)

To determine the organic matter content in the shell mineral, superficial shell organic matter, including the periostracum, was removed by submerging samples in a 50% (v/v) bleach bath for 1 h and then rinsing thoroughly three times with milli Q water, to ensure that no bleach residues remained. Samples were then dried out at 40 ºC overnight and then milled manually using an agate mortar and pestle. Alumina crucibles were empty weighted using a M2P microbalance (Sartorius, Germany) and then approximately 30 mg of powdered sample was placed inside. Then, samples were heated at 200 ºC, 400 ºC and 600 ºC for an hour in an oven (Hobersal model HD230, Forns Hobersal S.L., Spain). After each heating step, samples were allowed to cool down to room temperature, and their weight was recorded again.

### ICP-OES

To characterize shell mineral chemistry, shell samples were powdered and cleaned following the same protocol described for the TGA analysis. Afterwards, 10 mg of the sample were mixed with 0.5 ml of hydrogen peroxide, dissolved in nitric acid and then diluted with milli-Q water to a final concentration of 6.9% v/v. Samples were then filtered through a 0.22 µm Nylon syringe filter (Merck Millipore) and the concentration of Fe, Mg, Mn, Sr, Ba and Ca were measured using a Perkin-Elmer Optima 8300 mass spectrometer.

## Results

### Shell morphology

*A. purpuratus* shell has a macroscopic structure formed by radial ribs originating at the umbo, creating an undulated shell surface (Fig 1A). Shell coloration is varied, purple being the most common (Fig. 1 A), but also including brown and most rarely, white, yellow and orange (Winkler et al. 2001). The shell is equivalve and equilateral, with asymmetric auricles on the dorsal side (Fig. 1A). *A. purpuratus* has an alivincular and opisthodetic ligament and a disodont hinge (Fig. 1B). *A. purpuratus* is also a monomyarian bivalve, with only a posterior adductor muscle (Fig. 1B).

On the inner shell side, soft parts impressions are clearly visible (Fig. 1B). The pallial line marks the extension of the mantle attachment, while the more internal single adductor muscle scar is clearly visible as well. On the other hand, the pedal muscle scar, located behind that of the adductor muscle, is less conspicuous (Fig. 1B).

At the outer shell side, there is a series of superposed flanges running parallel to the growth margin. In the observed specimens, these terraces elevate at a ~45º angle with the shell surface and are more conspicuous at the flanks of the radial ribs. These structures can be clearly distinguished both under optical microscopy (e.g. Fig. 2B and D) and at low magnification under SEM (Fig. 3A and B). On transversal cross sections, the outer rib side is convex, whereas the inner part is concave. Troughs running parallel to shell ribs have a slightly concave outer side and a flat inner side (Figs. 2B and D).

**Shell microstructure**

Based on optical, mineralogical, and crystallographic data, the *A. purpuratus* shell can be divided into three main layers across its thickness. The outermost layer (Layer 1, hereafter) has a thickness of around 120 µm. The darker brownish hue indicates more organic matter occluded in this mineral layer when viewed under the optical microscope (Fig. 2A). SEM and EBSD observations reveal that it has a granular microstructure formed by small calcite crystals (Fig. 3E and Fig. 4A) with an average diameter of ~7.7 ± 2.5 µm.

The second layer (Layer 2 hereafter) of around 380 µm in thickness, appears to be composed of large, blocky calcite crystals under both optical microscopy (Fig. 2C) and EBSD (Fig. 4). However, closer inspection under SEM reveals that those crystals are small, tablet-like crystals with coherent crystallographic orientations (Fig. 3G) that cluster together in packs of coherent crystallographic orientations (Fig. 3F). Those packs measure up to 200×40 µm, with an average size of 96.5 × 27.5 µm along the longest and shortest diameters, respectively. These packs are oriented with their *c*-axes inclined at about 45° to the shell surface (Figs. 4 A and B).

The third, innermost layer (Layer 3, hereafter) is the thickest (around 850 µm), with a microcrystalline appearance that, under the optical microscope (polarized light), presents different colors due to their varying crystal orientations (Fig. 2C). It exhibits a foliated calcite microstructure, composed of elongated parallel platy crystals, or laths, which coalesce laterally to form sheets (folia). These laths have a diameter of 8.1 ± 2.3 µm and are arranged in superimposed lamellae of opposing orientation (Figs. 3H and I). Calcite laths within each lamella, however, display a high degree of co-orientation with a grain orientation spread (GOS) of less than 7°, as evidenced by the homogeneous color in the inverse pole figure (IPF) map (Fig. 4A). Each lath ends in well-defined rhombohedral {104} faces (Fig. 3J). Under optical microscopy, crystals at the bottom of this layer form a ~30º angle with the shell inner surface (Fig. 2A and C).

Transversal shell cross-sections (i.e., parallel to the shell margin) (Figs. 2B, D) observed under the optical microscope show the same general three-layer arrangement as well (Figs. 2B, D, and 4F). Polarized light observations reveal that crystals curve along their length, although the curvature does not follow that of the shell's surface, but maintain an angle with it (Fig. 2D). EBSD maps of transversal shell sections of *A. purpuratus* also show well differentiated layers with distinct microstructural characteristics and crystallographic arrangements (Figs. 4F). Layer 1 (155 ± 33 µm thick) contains fine equiaxed grains that progressively get into larger, irregularly shaped grains with an average size is 20.5 ±

5.3 µm. The topmost crystals within this layer exhibit no clear preferential orientation. Below them, larger grains start showing some ordering, with preferred rotation angles around their *c*-axis close to 60° (Fig. 4G). The distribution of the maximum misorientation within a grain was calculated relative to the mean grain reference orientation deviation (GROD), for which the maximum GROD reaches 31°.

Layer 2 (approx. 327 ± 17 µm thick) is composed of packs of calcite crystals that due to their coherent crystallographic orientations, appear in the EBSD maps as larger and elongated calcite crystals (128.8×37.5 µm) that diverge at 45° on either side from the shell surface (Fig. 4B). They likely correspond to fan-like calcite crystals observed by SEM in Layer 2 of the longitudinal cross-section (Fig. 3F and G). An increase in misorientation within a grain, indicated by a GOS of up to 18°, is observed as the grain expands. The remaining shell thickness (507 ± 22 µm) corresponds to Layer 3, characterized by a foliated calcite microstructure composed of very thin, elongate parallel crystals (laths, 3-5 µm thick) that form curved lamellae. These lamellae display a high degree of co-orientation, as evidenced by the uniform color in EBSD maps and the moderate crystallographic texture observed in the calculated pole figures (PFs) (Fig. 4G). About every 50 µm or so, there are marked changes in the crystallographic orientation of these sheets, as seen by shifting color gradients. Two distinct sets of folia are present (red and white arrows in Fig. 4G, bottom pole figure), which have their *c*-axis rotated about 35°, relative to each other, as indicated by the split maximum in the {001} pole figure. The three-layer arrangement is maintained regardless of specimen shell size (Fig. S4).

The characteristic shell three-layer arrangement is altered towards the dorsal shell side due to the presence of both the pallial and adductor myostraca. The adductor myostracum layer goes from the pallial margin and the adductor muscle insertion and then dips towards the interior of the shell in the direction of the umbo. This layer has a thick (110 µm) appearance under SEM (Figs. 3K and L) with a prismatic microstructure of aragonite crystals (Fig. 3L). The topmost section of the myostracum, is composed of an aragonitic high angle cross-lamellar microstructure (Fig 3M), originating a chevron-like microstructure (Fig. 3N). Below the myostracum there is a complex foliated layer (Figs. 3O and P). In this layer, calcite laths follow a more intricated arrangement, having several alternating directions, instead of just two alternating directions of the regular foliated layer. This complex foliated layer covers the inner shell surface inside the pallial line in those places where the myostracum does not crop out.

**Shell mineralogy and crystal orientation**

The three shell layers observed through microscopy also exhibit distinct crystallographic arrangements, which are clearly visible in the IPF maps obtained from both longitudinal and transversal cross-sections (Fig. 4 C and G). The variation in crystallographic texture across the shell thickness is reflected in the multiples of uniform density (MUD) values calculated for each region. MUD values range from about 15 to 50, indicating a generally strong but variable crystallographic texture among the layers.

In Layer 1, relatively low MUD values are observed (MUD = 15 and 24.4 in longitudinal and transversal cross sections, respectively), suggesting a weakly developed crystallographic preferred orientation compared to the underlying layers. This interpretation is consistent with the graphical representation of

the crystallographic texture shown in the PFs for Layer 1 (Fig. 4C). In Layer 2, the MUD value increases to 26.9 in the longitudinal cross-section and decreases to 16.6 in the transverse one. Although these domains appear as single-like grains in the EBSD maps, packs of crystals in the second layer have a GOS of up to 11°, indicating small misorientations between the individual crystals that compose those packs. In Layer 3, higher MUD values (MUD = 50 and 23 for longitudinal and transversal cross sections, respectively) occur in its upper part, where the calcite fibers are organized into broad, well-defined sheets with similar orientation and size (Fig. 4F). MUD values progressively decrease towards the inner shell surface, although they show a secondary increase from 16 to 26 in the region closest to the inner shell side in the longitudinal cross section (Fig 4D).

XRD analysis of *A. purpuratus* shell shows that calcite is the only mineral phase detected (Fig. S1), with the exception of the myostracum, which is made of aragonite (Guichaoua et al. 2025). Pole figures determined from 2D-DRX data revealed that calcite crystals are differentially oriented in the outer or inner surface of *A. purpuratus* shell (Fig. S2). In the outer shell side, pole figures do not show any well-defined preferential orientation and display either small, scattered maxima from single calcite crystals or very broad ill-defined maxima, indicating that the outer layer is more disorganized and formed by larger and more randomly oriented crystals (Fig. S2A). In contrast, pole figures at the inner surface show better defined maxima indicating that the inner layer is formed by packages of smaller calcite crystals with a preferential orientation (Fig. S2 B). The relatively small angular spread of these maxima of 19.4º indicates that calcite crystals have a high degree of co-orientation as observed by EBSD measurements. Note, however, that XRD data show a higher degree of disorientation of calcite crystals making the shell than EBSD data, as X-rays probe a substantially larger volume of the sample than EBSD measurements.

The chemistry of *A. purpuratus* shell calcitic minerals was also characterized by ICP-OES and TGA. ICP-OES indicated that Mg/Ca and Sr/Ca ratios in calcite were about 4.4 to 6.4 mmol/mol and 1.5 to 1.8 mmol/mol, respectively. On the other hand, Fe, Ba and Mn concentrations were below the instrument's detection limit of 0.1 ppm. Mg ionic substitution in the calcite structure estimated from unit cell parameters refined from XRD data by Rietveld method was almost negligible (< 0.1 % or < 1 mmol/mol) indicating that the shell mineral is made of nearly pure calcite with a very low Mg content (dos Santos et al. 2017). On the other hand, total organic matter within the shell mineral, as revealed by TGA, was relatively high (average of 3.7 ± 0.2 %), although its abundance has been seen to significantly change related to environmental factors (Ramajo et al., 2025). We also studied whether the incorporation of organic matter in the shell mineral modifies the calcite structure by comparing the unit cell parameters of the shell mineral to those of the mineral freed from organic matter by heating the samples at 400 °C. We observed an anisotropic increase of unit cell parameters, with the increase being larger along the c-axis (up to 0.08 %) than along the a-axis (up to 0.06 %), confirming a substantial modification in the calcite structure due to incorporation of organic matter incorporation.

When samples are heated at 400 ºC, there is a small, though non-significant increase in crystallite size from an average of 90.06 ± 7 nm to 94.82 ± 3 nm. Rietveld amorphous quantification was also very low

(between 2.5% to 0.3%), indicating the presence of very small or neglectable amounts of either amorphous mineral phases (e.g., ACC) or organics in the mature shell.

**Periostracum nanostructure and chemical composition**

SEM observation of the shell outer surface (Fig. 3A and B) at high magnification revealed the presence of a very thin periostracum forming a veil over the outermost shell mineral layer (Fig. 3C) with a fibrous wavy structure (Fig. 3D). Due to the lower electronic density of this organic coating, it has a good contrast (darker) with the underlying mineral layer (brighter) (Fig. 3C) when viewed under backscattered electrons.

Periostracum observations in cross-section using TEM confirmed that it is very thin, with a thickness ranging from ~200 nm to ~850 nm (Fig. 5A). It lacks any internal structure, presenting a very homogeneous appearance (Fig. 5B). The outer surface was dotted with regularly spaced protuberances with an average diameter of ~150 nm that give it a nanogranular appearance when observed under SEM (Fig. 3D). The inner side was wavy (Fig. 5B), originating much of the thickness variability and is delimited by a dark line strongly stained by $OsO_4$ (Fig. 5B).

The periostracum chemical composition was studied by infrared spectroscopy. ATR-FTIR spectra of the outer shell surface. It showed that the periostracum contributed to small amide bands at 1640 and 1540 $cm^{-1}$, associated with proteins, and a broad C-O-C band, around 1100 $cm^{-1}$, associated to polysaccharides. The very strong carbonate bands at around 1400, 874 and 710 $cm^{-1}$ were produced by the underlying shell (calcitic) mineral (Fig. S3). These data indicate that the periostracum is very thin and that its main chemical components are proteins, representing 7.3 to 9.4%, and polysaccharides (chitin; 1.8 to 7.2%).

# Discussion

The clade Bivalvia possesses a wealth of shell microstructures, with more than fifteen currently described. The best-known microstructures include nacre, prismatic, foliated and cross lamellar, with several microstructures generally present in the same shell (Checa 2018). These shell microstructures are usually made of aragonite, with calcite, if present, being always deposited in external layers. Shell mineral composition and microstructural organization are under biological control as each species produces a shell with unique and largely constant characteristics (Carter 1990a; Addadi et al. 2006).

The characterization of *A. purpuratus* shell microstructures has revealed that this organism has three well-defined shell layers with distinguishable microstructures. A granular microstructure on the outside (Layer 1), a middle layer composed of tablet-like crystals packed in granules of coherent crystallographic orientation (Layer 2), and an inner foliated layer which has the greatest contribution to the shell thickness (Layer 3). This three-layer pattern increases complexity towards the dorsal shell side with the appearance of two additional layers: the aragonite myostracum and a complex foliated layer underneath. In the superfamily Pectinoidea, there is an evolutionary trend to progressively replace simple prismatic

calcitic outer layers and cross lamellar aragonite layers with calcitic granular and foliated structures (Carter 1990a; Esteban-Delgado et al. 2008). In this evolutionary context, the outer granular calcitic microstructure observed in *A. purpuratus* may represent a vestigial structure from an ancestral calcitic prismatic microstructure (Carter 1990a). Well-developed foliated layers are commonplace within extant organisms of the order Pectinida (Esteban-Delgado et al., 2008). In fact, the three-layered shell structure is found in species closely related to *A. purpuratus,* such as *Argopecten irradians* or *Chlamys opercularis* (Carter 1990b). Similarly to *A. purpuratus*, *A. irradians* has an outer calcitic shell layer with a cross-foliated sublayer that transitions into a foliated sublayer. Underneath, there is an aragonitic cross-lamellar structure, that contains a columnar prismatic myostracum, 80 µm thick, with a complex cross-foliated layer below (Carter 1990b). In other related species, like *Chlamys opercularis*, polygonal simple calcitic prisms have also been reported at the outermost shell side of the right valve, but not on the left valve of juvenile specimens (Carter 1990b). In this species, irregular foliated to complex foliated structures have been reported above the pallial myostracum, whereas most of the inner shell exhibits an irregular complex foliated microstructure (Carter 1990b). Although less closely related to *A. purpuratus*, *Pecten maximus* also has a well-developed calcitic foliated structure (Grefsrud et al. 2008; Guichaoua et al. 2025), with a complex foliated layer also occurring underneath the myostracum (Guichaoua et al. 2025).

*A. purpuratus* foliated layers also share commonalities with foliated layers in ostreids. For instance, individual sheets have a single orientation, while there is slight variation in crystallographic axis orientation within each sheet (Sancho Vaquer et al. 2025). Furthermore, foliated units overlay each other in alternating orientations, forming roughly a 30º angle with the preceding foliated unit. In addition, in the {001} pole figure from Layer 3 (Fig. 4G) there are two well-defined sets of {001} broad maxima corresponding to each set of curved layers in which calcite crystals have their c-axis nearly perpendicular to the layering. Previous studies have also seen that the main surfaces of laths in pectinids and oysters range from {1 0 15} to {1 0 20}, at a high angle to the c-axis(Checa et al. 2019). This may indicate an annular arrangement of foliated laths, akin to the structure described for the foliated layers in ostreids (Checa et al. 2018; Sancho Vaquer et al. 2025).

EBSD analyses confirm that the calcitic shell is organized into three distinct layers, each characterized by specific microstructural and crystallographic arrangements. MUD values range from approximately 10 to 50, indicating a weak to strong texture that varies systematically across the shell layers. In the initial stage of growth, crystals nucleate independently, leading to weak preferred orientations in the outer granular layer. An MUD maximum is observed at the interface between Layer 2 and Layer 3 in both transversal and longitudinal cross-sections. Subsequently, the MUD decreases toward the inner shell surface (Figs. 4D and H), indicating a weakening of the overall crystallographic texture deeper within Layer 3.

Transversal sections viewed under EBSD reveal that folia occurring within Layer 3 grow on curved stacks, with marked changes in crystallographic orientation occurring every 10 to 20 µm, as shown by progressive color gradients in the IPF maps (Figs. 4C and G). The lateral boundaries between the layered

stacks display zig-zag morphology. Interestingly, despite their curvature, individual lamellae maintain a homogeneous color in IPF maps, indicating that crystals (laths) share a high degree of co-orientation. The texture (MUD values of 15–20) remains relatively constant across most of this layer, supporting the interpretation that the foliated calcite retains a uniform crystallographic alignment while accommodating local curvature of the folia.

Properties of the calcite mineral forming the *A. purpuratus* shell are similar to those observed in other biominerals. For instance, there is a significant lattice anisotropic distortion produced by the incorporation of organics within the calcite structure (Pokroy et al. 2006; Rodríguez-Navarro et al. 2024). On the other hand, Mg content within the calcite is very low, as it has been reported in other pectinids as well (Zamarreño et al. 1995), with values similar to those found in *Mytilus edulis* (Freitas et al. 2008), but around an order of magnitude lower than those reported in the closely related *Pecten maximus* (Freitas et al. 2006, 2008). Since Mg-calcite is more soluble than calcite, low Mg content in *A. purpuratus* shell mineral could be advantageous for protecting the shell from dissolution in their natural environment, which is seasonally affected by upwelling of low pH waters (Mucci and Morse 1984; Ramajo et al. 2025). On the other hand, Sr ratios are similar to those observed in *Pecten maximus* (Freitas et al. 2006).

*A. purpuratus* periostracum is extremely thin (200 to 800 μm), which is characteristic of ostreids and other pectinids (Córdova-Rodríguez et al. 2022), with thicknesses of 200 nm also reported in other *Pecten* species as well (Clark 1976). This contrasts with other bivalve species such as *Mytilus edulis*, which has a periostracum thickness two orders of magnitude higher (~15 μm; Grenier, Román, Duarte, et al., 2020). Additionally, although the main periostracum components (protein and polysaccharides) are the same as those reported in other bivalves, their proportions notably differ. For instance, *Mytilus chilensis* has a periostracum with much higher protein content (around 30%), whereas its polysaccharide content is lower (around 0.05%) (Grenier et al. 2020) than in *A. purpuratus*. Although, at first glance, a thin periostracum might apparently have a limited functionality, previous studies have observed that periostracum secretion and chemistry in *A. purpuratus* are highly sensitive to environmental variability (Lagos et al. 2021; Ramajo et al. 2025, 2022). This points towards an important role, protecting the organism from dissolution. In addition, a thin periostracum may be energetically advantageous for the organism, since periostracum production requires a significant energy investment (Palmer 1992), allowing *A. purpuratus* to allocate energy to other functions, such as shell mineralization or reproduction.

# Conclusions

- *A. purpuratus* shell is organized into three main layers with distinct microstructural and crystallographic characteristics. The outermost layer is the thinnest, with a thickness of around 120 μm, and is made of granular calcite crystals and exhibits weak crystallographic texture. The second layer is around 400 μm thick, with small platelet-shaped calcite crystals packed in groups with shared crystallographic orientation, reflecting an increased degree of orientation control. The third layer is the thickest (~ 500μm) and is characterized by a foliated microstructure with a well-

developed but spatially variable crystallographic texture, which is commonly present in other species of the group Pectinoidea.

- The periostracum covering *A. purpuratus* shell is extremely thin (a few hundred nm), which is a shared characteristic with other pectinids and ostreids. It has a fibrous structure with regularly spaced protuberances, and it is mainly composed of proteins and polysaccharides. Its thinness may provide a balance between shell protection from environmental stressors (e.g. low pH) and energy savings.
- The *A. purpuratus* shell is entirely made of calcite, with the exception of the aragonitic myostracum, and has relatively low Mg content. The shell mineral has a relatively high organic content (around 3.7%), which is incorporated into the calcite crystal structure producing an anisotropic lattice distortion, greater along the *c*-axis than along the *a*-axis, suggesting the intercalation of organics between the alternating $CaCO_3$ layers in the calcite structure.

## Declarations

# Competing Interest Statement

The authors have no relevant financial or non-financial interests to disclose.

# Acknowledgements

Authors thank the personnel at the University of Granada Scientific Instrumentation Center for their technical assistance. Authors also appreciate the reviewers' comments and efforts to improve the original manuscript. ABS, CG, KB, ARN and AGC thanks financial support through Projects PID2023-146394NB-I00 (Spanish Ministry of Science, Innovation and Universities) and PCM 00092 (Consejería de Economía, Innovación, Ciencia y Empleo, CEICE, Junta de Andalucía, JA), as well as the Unidad Científica de Excelencia UCE-PP2016-05 of the University of Granada. ACG also acknowledges the Research Group RNM363 (CEICE, JA). LR Laura Ramajo acknowledges the support from FONDAP/ANID 1523A0002 (CR2). KB was also supported by the program "Excellence Initiative—Research University" for the AGH University of Krakow.

## References

1. Acosta-Jofré MS, Sahade R, Mendo J, González-Ittig RE, Laudien J, Chiappero MB (2020) Population genetic structure and demographic history of the scallop Argopecten purpuratus from Peru and Northern Chile: implications for management and conservation of natural beds. Hydrobiologia 847:11–26. doi: 10.1007/s10750-019-04048-5
2. Addadi L, Joester D, Nudelman F, Weiner S (2006) Mollusk shell formation: A source of new concepts for understanding biomineralization processes. Chemistry - A European Journal 12:980–

987. doi: 10.1002/chem.200500980

3. Bakit J, Burgos-Fuster V, Abarca A, Etchepare I, Illanes JE, Villasante S, Bonilla E, Rojas R, Dudouet B, Cortés N (2024) Scallop aquaculture growth: Four decades of economic policy in Chile. Mar Policy 163. doi: 10.1016/j.marpol.2024.106139
4. Brand AR (2016) Scallop ecology: Distributions and behaviour. In: Shumway SE, Parsons GJ (eds) Scallops: Biology, Ecology, Aquaculture, and Fisheries, 3rd edition. Elselvier, Amsterdam, pp 469–533
5. Carter JG (1990a) Evolutionary significance of shell microstructure in the Palaeotaxodonta, Pteriomorphia and Isofilibranchia (Bivalvia:Molusca). In: Carter JG (ed) Skeletal Biomineralization: Patterns, Processes and Evolutionary Trends. Van Nostrand Reinhold, New York, pp 136–297
6. Carter JG (1990b) Shell microstructural data for the Bivalvia. Part V. Order Pectinoidea. In: Carter JG (ed) Skeletal Biomineralization: Patterns, Processes and Evolutionary Trends. Van Nostrand Reinhold, New York, pp 363–389
7. Checa AG (2018) Physical and biological determinants of the fabrication of Molluscan shell microstructures. Front. Mar. Sci. 5: 353. https://doi.org/10.3389/fmars.2018.00353
8. Checa AG, Harper EM, González-Segura A (2018) Structure and crystallography of foliated and chalk shell microstructures of the oyster Magallana: The same materials grown under different conditions. Sci Rep. 8:7507 doi: 10.1038/s41598-018-25923-6
9. Checa AG, Yáñez-Ávila ME, González-Segura A, Varela-Feria F, Griesshaber E, Schmahl WW (2019) Bending and branching of calcite laths in the foliated microstructure of pectinoidean bivalves occurs at coherent crystal lattice orientation. J Struct Biol 205:7–17. doi: 10.1016/j.jsb.2018.12.003
10. Clark GR (1976) Shell growth in the marine environment: approaches to the problem of marginal calcification. Am Zool 16:617–626. https://doi.org/10.1093/icb/16.3.617
11. Córdova-Rodríguez K, Flye-Sainte-Marie J, Fernández E, Graco M, Rozas A, Aguirre-Velarde A (2022) Effect of low pH on growth and shell mechanical properties of the Peruvian scallop Argopecten purpuratus (Lamarck, 1819). Mar Environ Res. 177: 195639. doi: 10.1016/j.marenvres.2022.105639
12. dos Santos HN, Neumann R, Ávila CA (2017) Mineral quantification with simultaneous refinement of Ca-Mg carbonates non-stoichiometry by X-Ray diffraction, Rietveld method. Minerals 7:164. doi: 10.3390/min7090164
13. Esteban-Delgado FJ, Harper EM, Checa AG, Rodríguez-Navarro AB (2008) Origin and expansion of foliated microstructure in pteriomorph bivalves. Biological Bulletin 214:153–165. doi: 10.2307/25066672
14. Fernández-Reiriz MJ, Navarro JM, Labarta U (2005) Enzymatic and feeding behaviour of Argopecten purpuratus under variation in salinity and food supply. Comparative Biochemistry and Physiology - A Molecular and Integrative Physiology 141:153–163. doi: 10.1016/j.cbpb.2005.04.020
15. Freitas PS, Clarke LJ, Kennedy H, Richardson CA, Abrantes F (2006) Environmental and biological controls on elemental (Mg/Ca, Sr/Ca and Mn/Ca) ratios in shells of the king scallop Pecten maximus. Geochim Cosmochim Acta 70:5119–5133. doi: 10.1016/j.gca.2006.07.029

16. Freitas PS, Clarke LJ, Kennedy HA, Richardson CA (2008) Inter-and intra-specimen variability masks reliable temperature control on shell Mg/Ca ratios in laboratory-and field-cultured Mytilus edulis and Pecten maximus (Bivalvia). Biogeosciences 5:1245-1258. https://doi.org/10.5194/bg-5-1245-2008
17. Grefsrud ES, Dauphin Y, Cuif JP, Denis A, Strand Ø (2008) Modifications in microstructure of cultured and wild scallop shells (Pecten maximus). J Shellfish Res 27:633–641. doi: 10.2983/0730-8000(2008)27[633:MIMOCA]2.0.CO;2
18. Grenier C, Román R, Duarte C, Navarro JM, Rodríguez-Navarro AB, Ramajo L (2020) The combined effects of salinity and pH on shell biomineralization of the edible mussel Mytilus chilensis. Environmental Pollution 263:114555 doi: 10.1016/j.envpol.2020.114555
19. Guichaoua L, Reznikov N, Stewart BD, Kroger R, Gauvin R (2025) Combined crystallographic study of king scallop (Pecten maximus) shells using SEM, EBSD and Raman spectroscopy. Faraday Discuss 261:484-500 doi: 10.1039/D5FD00029G
20. Lagos NA, Benítez S, Duarte C, Lardies MA, Broitman BR, Tapia C, Tapia P, Widdicombe S, Vargas CA (2016) Effects of temperature and ocean acidification on shell characteristics of Argopecten purpuratus: Implications for scallop aquaculture in an upwelling-influenced area. Aquac Environ Interact 8:357–370. doi: 10.3354/AEI00183
21. Lagos NA, Benítez S, Grenier C, Rodríguez-Navarro AB, García-Herrera C, Abarca-Ortega A, Vivanco JF, Benjumeda I, Vargas CA, Duarte C, Lardies MA (2021) Plasticity in organic composition maintains biomechanical performance in shells of juvenile scallops exposed to altered temperature and pH conditions. Sci Rep. 11: 24201 doi: 10.1038/s41598-021-03532-0
22. Lamarck J-BM (1819) Histoire naturelle des animaux sans vertèbres. Published by the author, Paris. http://www.biodiversitylibrary.org/item/47441
23. Li C, Liu X, Liu B, Ma B, Liu F, Liu G, Shi Q, Wang C (2018) Draft genome of the Peruvian scallop Argopecten purpuratus. Gigascience 7:giy031 doi: 10.1093/gigascience/giy031
24. Marín A, Fujimoto T, Arai K (2013) Genetic structure of the Peruvian scallop Argopecten purpuratus inferred from mitochondrial and nuclear DNA variation. Mar Genomics 9:1–8. doi: 10.1016/j.margen.2012.04.007
25. Mendo J, Wolff M, Mendo T, Ysla L (2016) Scallop fishery and culture in Peru. In: Developments in Aquaculture and Fisheries Science. Elsevier, pp 1089–1109. https://doi.org/https://doi.org/10.1016/B978-0-444-62710-0.00028-6
26. Mucci A, Morse JW (1984) The solubility of calcite in seawater solutions of various magnesium concentration, Zi = 0.697 m at 25°C and one atmosphere total pressure. Geochim Cosmochim Acta 48:815–822. doi: 10.1016/0016-7037(84)90103-0
27. Muñoz R, Vergara OA, Figueroa PA, Mardones P, Sobarzo M, Saldías GS (2023) On the phenology of coastal upwelling off central-southern Chile. Dynamics of Atmospheres and Oceans 104:101405. doi: 10.1016/j.dynatmoce.2023.101405
28. Palmer RA (1992) Calcification in marine molluscs: How costly is it? Proceedings of the National Academy of Sciences 89:1379–1382. doi: 10.1073/pnas.89.4.1379

29. Pokroy B, Fitch AN, Marin F, Kapon M, Adir N, Zolotoyabko E (2006) Anisotropic lattice distortions in biogenic calcite induced by intra-crystalline organic molecules. J Struct Biol 155:96–103. doi: 10.1016/j.jsb.2006.03.008
30. Produce (2025) Ficha técnica: Recurso concha de abanico – Año 2024. https://www.producempresarial.pe/wp-content/uploads/2025/02/256-Ficha-632 Recurso-Concha-abanico-Ano-2024.pdf
31. Ramajo L, Marbà N, Prado L, Peron S, Lardies MA, Rodríguez-Navarro AB, Vargas CA, Lagos NA, Duarte CM (2016) Biomineralization changes with food supply confer juvenile scallops (Argopecten purpuratus) resistance to ocean acidification. Glob Chang Biol 22:2025–2037. doi: 10.1111/gcb.13179
32. Ramajo L, Valladares M, Astudillo O, Fernández C, Rodríguez-Navarro AB, Watt-Arévalo P, Núñez M, Grenier C, Román R, Aguayo P, Lardies MA, Broitman BR, Tapia P, Tapia C (2020) Upwelling intensity modulates the fitness and physiological performance of coastal species: Implications for the aquaculture of the scallop Argopecten purpuratus in the Humboldt Current System. Science of the Total Environment 745:140949 doi: 10.1016/j.scitotenv.2020.140949
33. Ramajo L, Sola-Hidalgo C, Valladares M, Astudillo O, Inostroza J (2022) Size matters: Physiological sensitivity of the scallop Argopecten purpuratus to seasonal cooling and deoxygenation upwelling-driven events. Front Mar Sci. doi: 10.3389/fmars.2022.992319
34. Ramajo L, Rodríguez-Navarro AB, Brokordt K, Barry-Sosa A, Jeno K, Sola-Hidalgo C, Valladares M, Inostroza J (2025) Nutritional status and shell properties of the scallop Argopecten purpuratus are sensitive to intense upwelling events. Mar Environ Res 210:107322 doi: 10.1016/j.marenvres.2025.107322
35. Rodríguez-Navarro AB, Domínguez-Gasca N, Athanasiadou D, Le Roy N, González-Segura A, Reznikov N, Hincke MT, McKee MD, Checa AG, Nys Y, Gautron J (2024) Guinea fowl eggshell structural analysis at different scales reveals how organic matrix induces microstructural shifts that enhance its mechanical properties. Acta Biomater 178:244–256. doi: 10.1016/j.actbio.2024.03.001
36. Sancho Vaquer A, Griesshaber E, Salas C, Harper EM, Checa AG, Schmahl WW (2025) The diversity of crystals, microstructures and texture that form Ostreoidea shells. Crystals 15:286. doi: 10.3390/cryst15030286
37. Sernapesca (2024) Anuarios estadísticos de pesca y acuicultura. https://www.sernapesca.cl/informacion-utilidad/anuarios-estadisticos-de-pesca-y-666 acuicultura/
38. Soria G, Merino G, von Brand E (2007) Effect of increasing salinity on physiological response in juvenile scallops Argopecten purpuratus at two rearing temperatures. Aquaculture 270:451–463. doi: 10.1016/j.aquaculture.2007.05.018
39. Taylor MH, Wolff M, Vadas F, Yamashiro C (2008) Trophic and environmental drivers of the Sechura Bay ecosystem (Peru) over an ENSO cycle. Helgol Mar Res 62:15–32. doi: 10.1007/s10152-007-0093-4

40. Winkler FM, Estevez BF, Jollan LB, Garrido JP (2001) Inheritance of the general shell color in the scallop Argopecten purpuratus (Bivalvia: Pectinidae). The Journal of Heredity 92:521–525.
41. Wolff M, Mendo J (2000) Management of the Peruvian bay scallop (Argopecten purpuratus) metapopulation with regard to environmental change. Aquat Conserv 10:117–126. doi: 10.1002/(SICI)1099-0755(200003/04)10:2<117::AID-AQC399>3.0.CO;2-T
42. Yáñez E, Lagos NA, Norambuena R, Silva C, Letelier J, Muck K, Martin GS, Benítez S, R. Broitman B, Contreras H, Duarte C, Gelcich S, Labra FA, Lardies MA, Manríquez PH, Quijón PA, Ramajo L, González E, Molina R, Gómez A, Soto L, Montecino A, Barbieri MÁ, Plaza F, Sánchez F, Aranis A, Bernal C, Böhm G (2017) Impacts of Climate Change on Marine Fisheries and Aquaculture in Chile. In: Phillips BF, Pérez-Ramírez M, Phillips BF, Pérez-Ramírez M (eds) Climate Change Impacts on Fisheries and Aquaculture. John Wiley & Sons, Ltd, Chichester, UK, pp 239–332
43. Zamarreño I, De Porta J, Vázquez A (1995) The shell microstructure, mineralogy and isotopic composition of Amussiopecten (Pectinidae, Bivalvia) from the Miocene of Spain: A valuable paleoenvironmental tool. GEOBIOS 6:707–724. https://doi.org/10.1016/S0016-6995(96)80017-9

# Figures

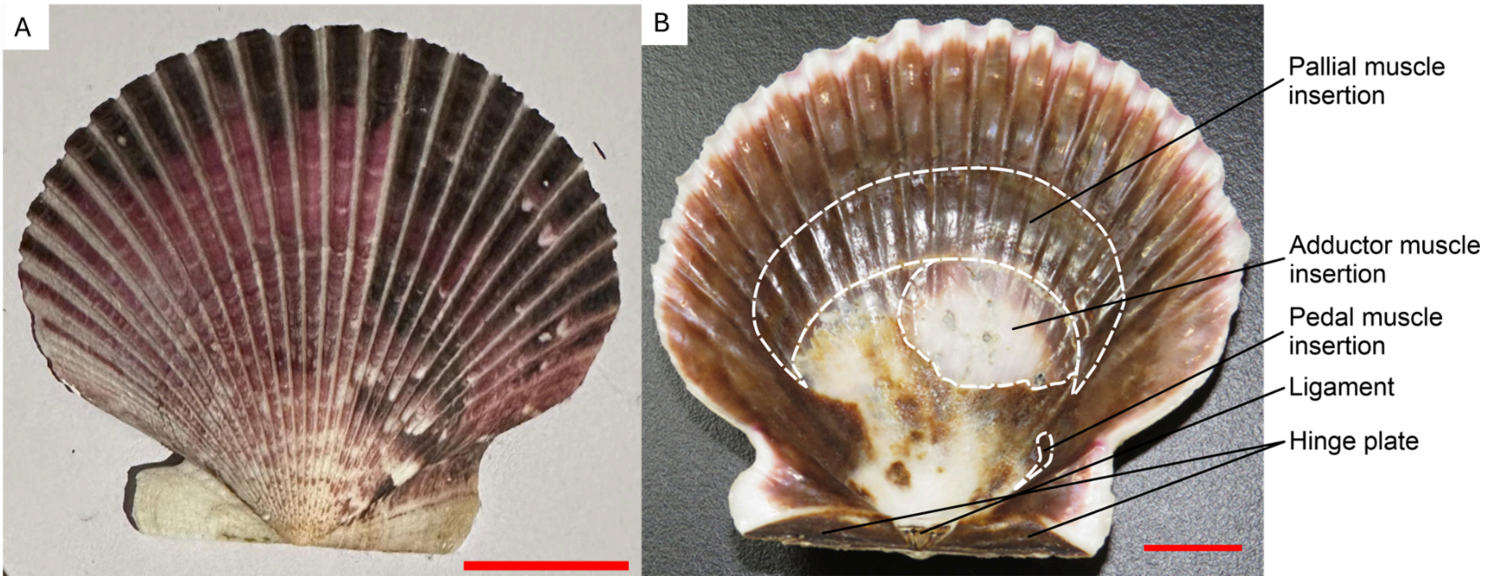



**Figure 1**

Macroscopical appearance of *Argopecten purpuratus*: **A.** Outer surface, showing the radial ribs and the typical purple coloration. **B.** Inner surface, with the adductor and pallial muscular impressions indicated. Scale bars: **A.** 3 cm, **B.** 1 cm.

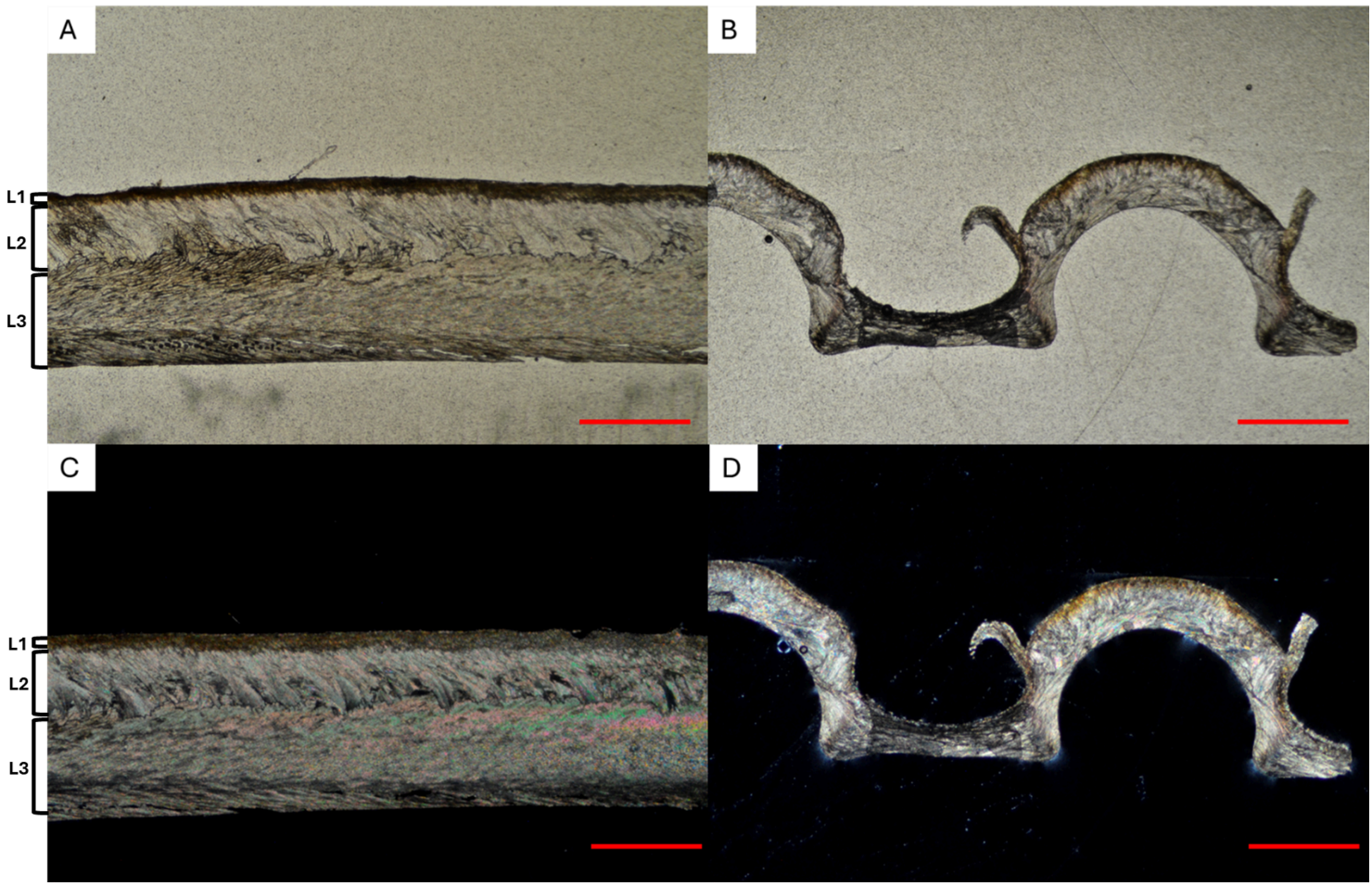



**Figure 2**

*Argopecten purpuratus*sections under the optical microscope (sample 65R; small individual, length = 40 mm): **A.** and **C.**: Longitudinal cross-sections of the shell viewed under parallel (white background) and cross-polarized light (black background), respectively. **B.** and **D.**: Transversal cross-sections of the shell viewed under parallel and cross-polarized light. In A. and C., L1, L2 and L3 denotes Layer 1, Layer 2 and Layer3, respectively. Scale bars: 750 µm.

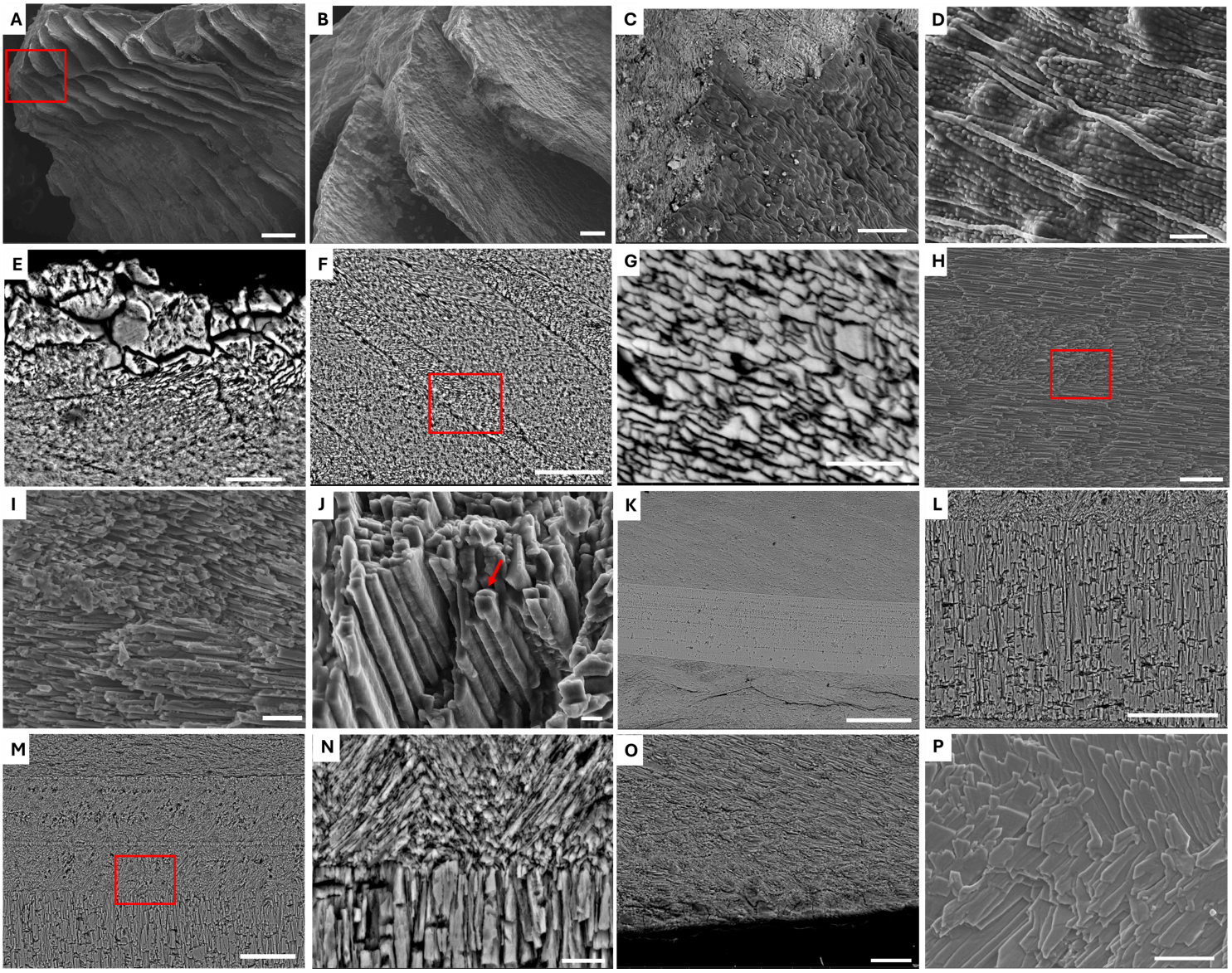
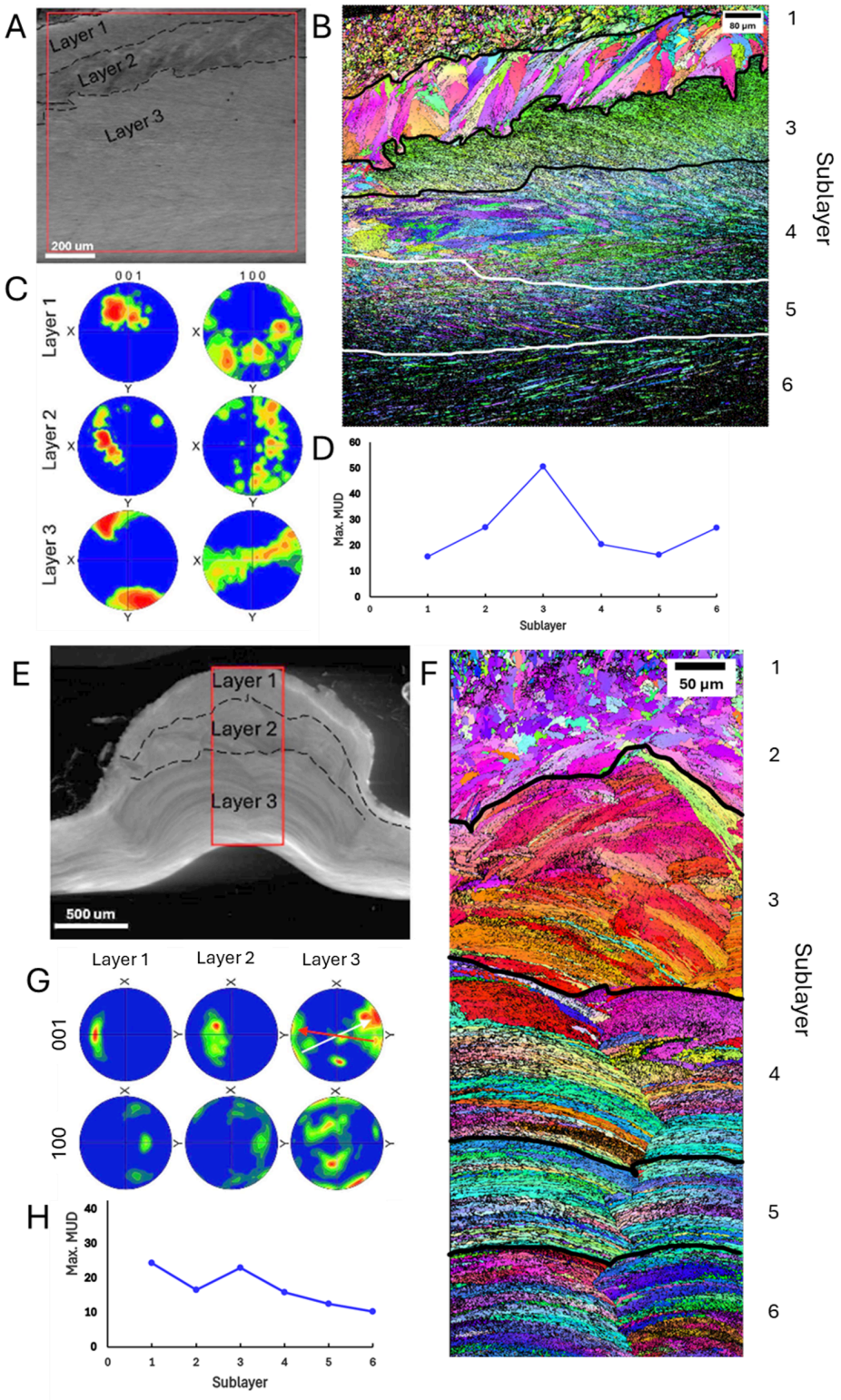



**Figure 3**

SEM images of *A. purpuratus* shell. **A.**External view of *A. purpuratus* shell. **B.** Detailed view of the transversal terraces squared in A. **C.** Backscattered electron image of the shell surface, partially covered by the periostracum (right side, darker color). **D.** Detailed view of the periostracum surface, depicting its fibrous structure. **E.** Layer 1 in longitudinal section, showing a blocky structure. **F.** Co-oriented packs of calcite crystals located underneath the layer in E. **G.** Detail of the material squared in F. **H., I.**Foliated calcitic layer, showing superposed layers of laths with opposite directions. I. is a closer view of the region squared in H. **J.** Detail of calcite laths in the foliated layer. The red arrow shows an example of rhombohedral faces. **K.** Backscattered electron image showing a general view of the myostracum. **L.** Detail of myostracal prisms. **M., N.**View of the cross lamellar layer that forms the top part of the myostracum. **N.** Detail of the cross lamellar layer indicated by the square in M. **O.** Irregular foliated layer located below the myostracum. **P.** Surface view of the calcite laths of the irregular foliated material. Scale bar **A.** 500 µm **B.** 50 µm **C.**10 µm **D.** 2 µm **E.** 10 µm **F.** 20 µm **G.** 3 µm **H.**10 µm **I.** 2.5 µm **J.** 500 nm **K.** 200 µm **L.** 50 µm **M.**50 µm **N.** 5 µm **O.** 25 µm **P.** 5 µm.




## Figure 4

*A. purpuratus* shell microstructure analyzed by EBSD for (**A-D**) longitudinal and (**E-H**) transversal shell cross-section. The microstructure of the three shell layers and the regions mapped for EBSD (red squares) are indicated in the SEM images (**A** and **E**). The inverse pole figure (IPF) maps (**C**and **G**) show the crystallographic orientation of calcite grains of layers 1 to 3. In G, the arrows (red and white) in the {001} pole figure of layer 3 indicate the two predominant orientations of calcite *c*-axes. The evolution of

the degree of crystal preferential orientation (in MUD units) as a function of shell thickness is plotted in **D**and **H**.

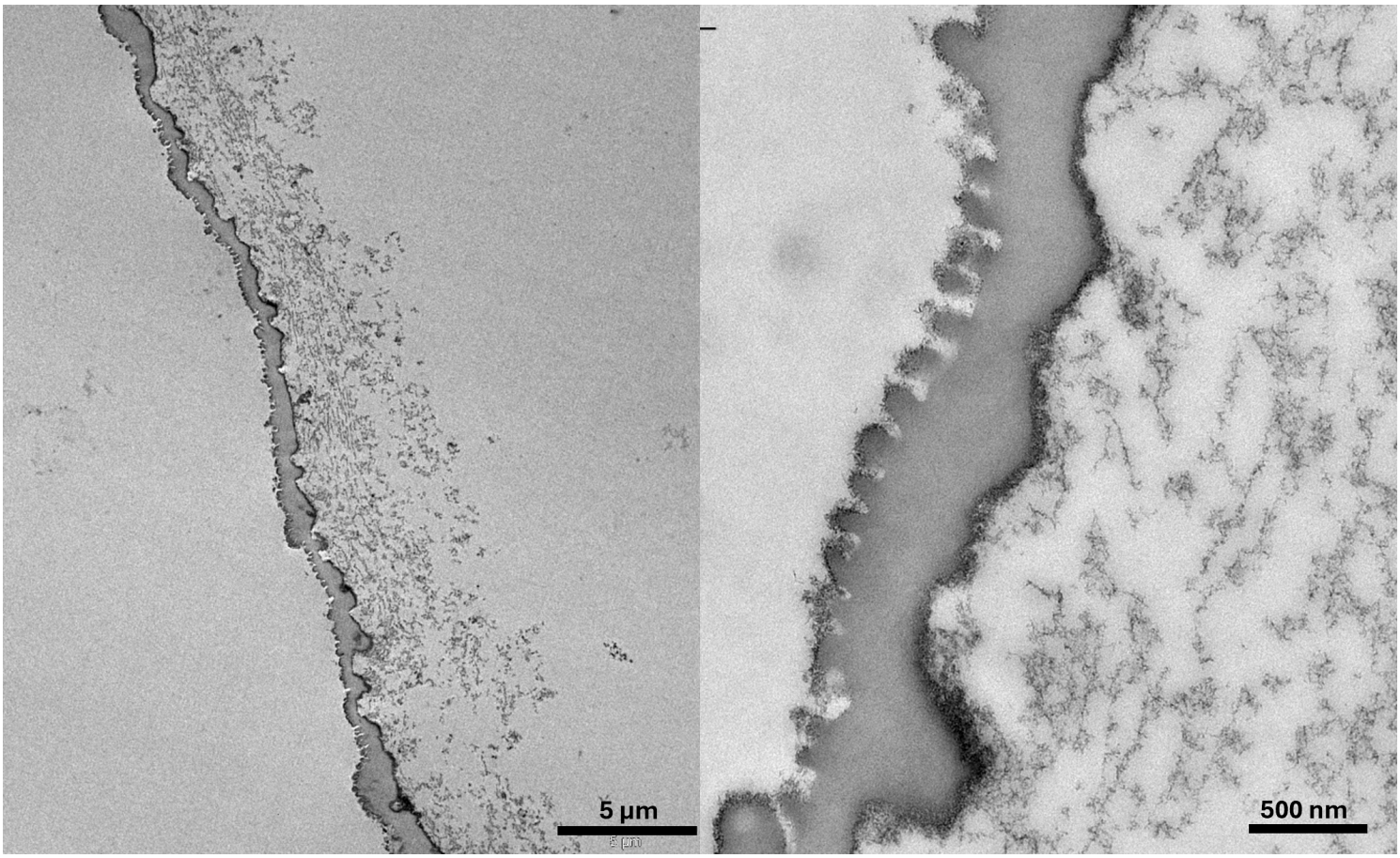



**Figure 5**

TEM images of *A. purpuratus* periostracum. **A.** General view. Note the changes in thickness across its length. **B.** Close up showing protuberances on the outer side. Note organic remains left after the shell dissolution. Outer periostracum surface to the left of both images.

## Supplementary Files

This is a list of supplementary files associated with this preprint. Click to download.

- SUPPLEMENTARYMATERIALS.pdf